PCCP

PAPER

View Article Online
View Journal

Cite this: DOI: 10.1039/c4cp00460d

Depletion region effect of highly efficient hole conductor free $CH_3NH_3PbI_3$ perovskite solar cells

Sigalit Aharon, Shany Gamliel, Bat El Cohen and Lioz Etgar*

Received 30th January 2014,
Accepted 7th April 2014

DOI: 10.1039/c4cp00460d

www.rsc.org/pccp

The inorganic–organic perovskite is currently attracting a lot of attention due to its use as a light harvester in solar cells. The large absorption coefficients, high carrier mobility and good stability of organo-lead halide perovskites present good potential for their use as light harvesters in mesoscopic heterojunction solar cells. This work concentrated on a unique property of the lead halide perovskite, its function simultaneously as a light harvester and a hole conductor in the solar cell. A two-step deposition technique was used to optimize the perovskite deposition and to enhance the solar cell efficiency. It was revealed that the photovoltaic performance of the hole conductor free perovskite solar cell is strongly dependent on the depletion layer width which was created at the TiO_2–$CH_3NH_3PbI_3$ junction. X-ray diffraction measurements indicate that there were no changes in the crystallographic structure of the $CH_3NH_3PbI_3$ perovskite over time, which supports the high stability of these hole conductor free perovskite solar cells. Furthermore, the power conversion efficiency of the best cells reached 10.85% with a fill factor of 68%, a V_{oc} of 0.84 V, and a J_{sc} of 19 mA cm^{-2}, the highest efficiency to date of a hole conductor free perovskite solar cell.

Introduction

The search for alternative energy solutions is currently a leading research area and will remain so for the foreseeable future, and photovoltaics (PV) are a key technology for a sustainable energy supply. The basic requirement for PV devices is the charge separation of electrons and holes in a material, which absorbs the light, and the conductivity of these charges to different contacts.

A recent breakthrough was made by using a new light absorber, the inorganic–organic perovskite, in the solar cell. The inorganic–organic perovskite consists of an inorganic part, usually a divalent metal cation to satisfy the charge balancing. The organic part consists of an organic cation to form the three-dimensional perovskite structure.

The inorganic–organic perovskite has a direct band gap, large absorption coefficients[1] and high carrier mobility,[2,3] which present good potential for its use as a light harvester in mesoscopic heterojunction solar cells.

Several studies used the $CH_3NH_3PbI_3$ perovskite as a sensitizer in photoelectrochemical cells with a liquid electrolyte.[4–6] However, the performance of these systems rapidly declined due to dissolution of the perovskite. This problem was solved by replacing the electrolyte with a solid state hole conductor.[7] Moreover, the tin iodide-based perovskite $CsSnI_3$ has been employed as a hole conductor together with N719 as a sensitizer in solid state dye-sensitized solar cells, yielding a power conversion efficiency (PCE) of 8.5%.[8] Several reports showed[9–11] efficient hybrid organic–inorganic solar cells, based on a *meso*-superstructured organo-halide perovskite, yielding a power conversion efficiency of 10.9% to 12.3%.

A high open circuit voltage was demonstrated for these perovskite based solar cells, having V_{oc} of 1.15 V and 1.3 V.[12,13] Recently impedance spectroscopy was carried out on these high efficiency perovskite solar cells, the authors recognized charge accumulation in the absorber material (the perovskite) which derives from the capacitance of the devices.[14] Good correlation between the calculated electronic and optical band gap and the experimental results was found using theoretical modeling of the perovskite based halides.[15] In addition, the high efficiency achieved for the perovskite based solar cells was supported by measuring the long-range electron–hole diffusion length.[16,17]

Recently, more than 15% power conversion efficiency was reported. In one work a two step deposition technique of the perovskite was demonstrated[18] while in another work a co-evaporation deposition technique on a flat surface was used.[19] Besides this breakthrough, Etgar *et al.*[20] reported on the use of hole conductor free perovskite solar cells. The authors demonstrated for the first time that the perovskite can function as a light harvester and as a hole conductor at the same time. In early work 5% efficiency was reported and recently this performance was improved to 8% efficiency for depleted hole conductor free perovskite solar cells.[21] In addition a PCE of 10.49% was achieved for a hole conductor free perovskite solar cell.[22] Elimination of the

The Hebrew University of Jerusalem, Institute of Chemistry, Casali Center for Applied Chemistry, Israel. E-mail: lioz.etgar@mail.huji.ac.il

hole conductor can improve the stability, lower the cost and simplify the fabrication process.

In this research, we concentrated on using $CH_3NH_3PbI_3$ perovskite as a light harvester and as a hole conductor simultaneously in the solar cell. We performed a complete study of several parameters, which influence the PV performance of these hole conductor free lead halide iodide perovskite solar cells. We optimized the use of the two-step deposition technique of the perovskite, and we have found a correlation between the depletion layer width at the TiO_2–$CH_3NH_3PbI_3$ junction and the power conversion efficiency observed. X-Ray diffraction analysis revealed that there is no change in the crystallographic structure of the $CH_3NH_3PbI_3$ perovskite over time, indicating the high stability of these cells. Finally, the best power conversion efficiency (PCE) achieved in this work was 10.85%, the highest efficiency to date of a hole conductor free perovskite solar cell.

Results and discussion

This work concentrates on the use of lead halide perovskite as a light harvester and as a hole conductor simultaneously in the solar cell. The solar cell structure and its energy level diagram are shown in Fig. 3A and B, respectively, which consists of a blocking layer followed by the deposition of mesoporous TiO_2 film, perovskite film and gold as the back contact. The blocking layer has an important role as it improves the PV parameters of the solar cell. In this work, the blocking layer was fabricated by spin coating a solution of diluted titanium diisopropoxidebis-(acetylacetonate) (TiDIP) in ethanol, which permitted more control of the blocking layer thickness and density. The influence of the blocking layer on the PV performance was investigated by changing the blocking layer thickness and concentration. Table 1 presents the PCE of cells made under different blocking layer conditions (spin velocity (rounds per minute (rpm)) and the TiDIP precursor concentration). In order to study the influence of the blocking layer conditions on the PV performance all the other parameters were held constant.

The best PCE was observed for a spin velocity of 1500 rpm and 0.15% volume fraction of TiDIP under the blocking layer conditions. Looking at the results, it was observed that for each concentration, there is an optimal spin velocity. At low concentrations, the best efficiency was observed at low spin velocity. The spin velocity determines the blocking layer thickness, so when using low TiDIP concentration, a thick blocking layer is preferred (*i.e.* low spin velocity). On the other hand, at a high concentration of TiDIP, the best efficiency was observed at high spin velocity. The high spin velocity enables achieving a thin, uniform blocking layer, so that a high TiDIP concentration can be used. In the case of high TiDIP concentration and low spin velocity, a thick and condensed blocking layer was formed resulting in low PV performance.

Table 1 Efficiencies of the hole conductor free perovskite solar cells under different blocking layer conditions, *i.e.* spin velocity (rpm) and at various TiDIP concentrations

Volume fraction of TiDIP (%)	Spin velocity 500 rpm (%)	Spin velocity 1500 rpm (%)	Spin velocity 2500 rpm (%)
0.05	4.5	3.0	3.0
0.10	4.2	7.0	2.0
0.15	5.0	7.2	2.2
0.20	3.0	5.4	6.5

The deposition of the lead halide iodide perovskite on the mesoporous TiO_2 was done based on the two-step deposition method (spin and dip) described earlier[18] but with several modifications which assist in controlling the lead halide iodide perovskite deposition on the mesoporous TiO_2. The first step was spinning PbI_2 on the mesoporous TiO_2 film and annealing at 70 °C, while the second step was dipping the PbI_2 electrode into CH_3NH_3I solution. After PbI_2 reacts with CH_3NH_3I, $CH_3NH_3PbI_3$ was formed. An important step in this deposition technique is the wait time period after dropping the PbI_2 on the mesoporous TiO_2 film, before spinning. We investigated the wait time parameter and observed its influence on the PV parameters of these cells. The results are summarized in Fig. 1. The highest efficiency (8.0%) was achieved at a wait time of 3 minutes.

During 3 minutes of waiting time, PbI_2 creates a uniform coating on the mesoporous TiO_2 surface while a longer waiting time (5 min) causes evaporation of the PbI_2's solvent, which could create a non-uniform coating of the PbI_2 on the mesoporous TiO_2 surface. Conversely, the coverage of the surface by PbI_2 isn't complete during a too-short wait time.

The influence of the TiO_2 film thickness was investigated by making hole conductor free perovskite based solar cells using different thickness of mesoporous TiO_2 films while keeping the $CH_3NH_3PbI_3$ perovskite film thickness constant (the same deposition parameters were used for the perovskite deposition). To achieve different TiO_2 film thicknesses, the TiO_2 paste was diluted by ethanol at various ratios. The various dilutions produced different thicknesses of TiO_2 films as seen in Fig. 2A–E. The thickness of the mesoporous TiO_2 film was measured using the Dektak 150 profiler, and the results are shown in the Fig. 2E graph. Fig. 2A–D presents extra high resolution scanning electron microscopy (XHR-SEM) of the various TiO_2 thicknesses in the complete

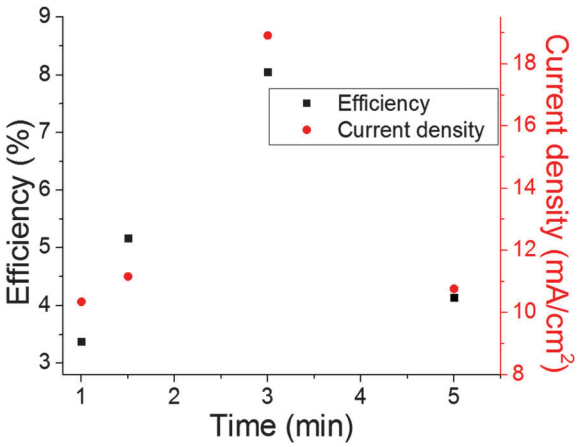

Fig. 1 The current density and the efficiency of the cells *versus* the wait time (min) between dropping PbI_2 until the beginning of the spinning.

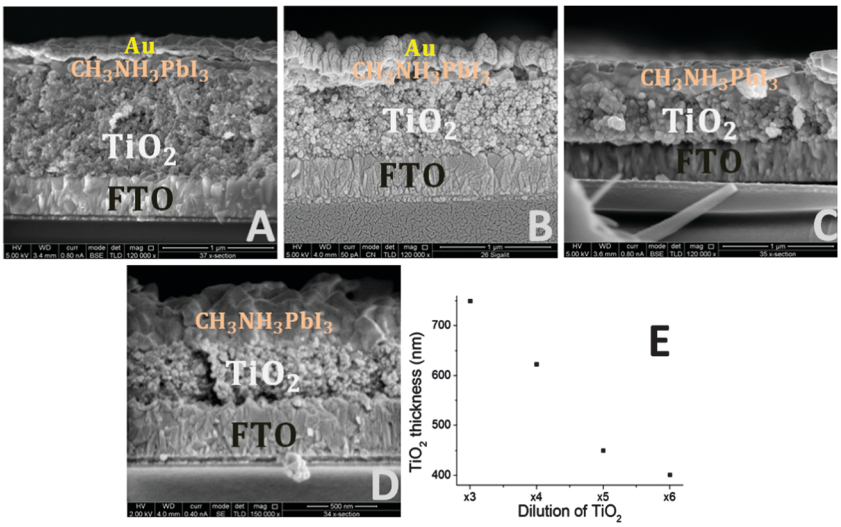

Fig. 2 XHR-SEM of the different TiO_2 thickness in the complete TiO_2–$CH_3NH_3PbI_3$ perovskite based solar cells. (A) The thicker TiO_2 film corresponds to 3 times dilution see (E). (B) 4 times dilution. (C) 5 times dilution. (D) 6 times dilution. Importantly the thickness was measured using a surface profiler, the results of which are shown in (E).

Table 2 PV performance of the hole conductor free TiO_2–$CH_3NH_3PbI_3$ perovskite based solar cells obtained for various TiO_2 film thicknesses

Thickness of TiO_2 film (nm) ± 25 nm	V_{oc} (V)	J_{sc} (mA cm^{-2})	FF	Efficiency (%)
750	0.66	12.47	0.45	3.7
620	0.73	16.03	0.61	7.2
450	0.68	13.27	0.63	5.7
400	0.65	10.47	0.55	3.8

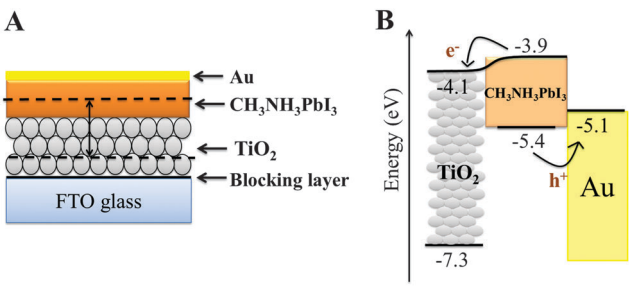

Fig. 3 (A) The structure of the hole conductor free TiO_2–$CH_3NH_3PbI_3$ perovskite based solar cells. The arrow indicates the depletion region observed at the TiO_2–$CH_3NH_3PbI_3$ junction. (B) Energy level diagram of the discussed solar cell which shows the charge separation process. The position of the energy levels is taken from ref. 20.

set of thicknesses of TiO_2–$CH_3NH_3PbI_3$ perovskite solar cells. It can be observed that $CH_3NH_3PbI_3$ formed an overlayer on top of the TiO_2 film. Probably some of the $CH_3NH_3PbI_3$ penetrated into the TiO_2 film, however the thick overlayer of the $CH_3NH_3PbI_3$ film (300 nm ± 50 nm) indicates that most of the perovskite stays on top of the TiO_2 film. Table 2 summarizes the results obtained for the solar cells made with various TiO_2 thicknesses. For each TiO_2 thickness more than 5 cells were fabricated in order to investigate the reliability of the presented results. The highest efficiency was observed for cells made with mesoporous TiO_2 film of 620 ± 25 nm thickness. In these cells, the current density and the open circuit voltage were higher than the other cells made with different thicknesses of TiO_2. The lowest efficiencies were observed for the thick TiO_2 film (750 ± 25 nm) and for the thin TiO_2 film (400 ± 25 nm). In addition, the FF and the current density for these cells were also the lowest compared with the other TiO_2 thicknesses.

To understand the reason for the difference in PV performance observed when using a variety of TiO_2 film thicknesses, capacitance voltage measurements were performed. In our previous work,[21] it was reported that a depletion layer is created in the $CH_3NH_3PbI_3$ perovskite film and in the TiO_2 mesoporous film. This depletion layer assists in the charge separation and inhibits the back reaction of electrons from the TiO_2 to the $CH_3NH_3PbI_3$ film. To estimate the depletion region width, Mott Schottky analysis[23] of the TiO_2–$CH_3NH_3PbI_3$ heterojunction solar cells was performed.

The capacitance at the junction which is described in eqn (1) is calculated from the depletion approximation.[24] The depletion approximation implies that there are no free carriers in the space charge region at the junction under investigation.

$$\frac{1}{C^2} = \frac{2}{\varepsilon\varepsilon_0 q A^2 N}(V_{bi} - V) \quad (1)$$

where C is the measured capacitance, A is the active area, V is the applied bias, ε is the static permittivity, ε_0 is the permittivity of free space, q is elementary charge and N is the doping density of the donor. The static permittivity of $CH_3NH_3PbI_3$ was measured and calculated to be 30.[25,26] From the slope of the Mott Schottky plot in the linear regime, the net doping density of the $CH_3NH_3PbI_3$ film can be calculated. Moreover, the intersection of the linear regime in the Mott Schottky plot with the x-axis determines the built-in voltage, which suppressed the back reaction of electrons from the TiO_2 film to the $CH_3NH_3PbI_3$ film.

Table 3 Calculated depletion width and the built-in potential for various TiO_2 film thicknesses

Thickness of TiO_2 (nm) ± 25 nm	Depleted TiO_2[a]	V_{oc} (V)	V_{bi} (V)	Efficiency (%)	W_t (nm)	W_n (nm)	W_p (nm)
750	0.12	0.66	0.87	3.8	223	88	135
620	0.49	0.73	0.74	7.2	395	306	89
450	0.31	0.68	0.70	5.7	239	140	99
400	0.10	0.65	0.73	3.7	194	44	150

[a] The "depleted TiO_2" is the fraction of the part in the TiO_2 film that is depleted. More than 5 cells were fabricated for each condition.

The depletion width is calculated according to:[27]

$$W_{p,n} = \frac{1}{N_{a,d}}\sqrt{\frac{2\varepsilon V_{bi}}{q\left(\frac{1}{N_a + N_d}\right)}} \quad (2)$$

where N_a and N_d are the doping densities of the acceptor and the donor, respectively. Literature values of doping density in nanoporous TiO_2 start at $N_a = 1 \times 10^{16}$ cm^{-3}.[28–30]

Table 3 summarizes the calculated W_n, W_p, total depletion width (W_t) and the built-in potential (V_{bi}) for the various TiO_2 film thicknesses.

The correlation between the power conversion efficiency for the various TiO_2 film thicknesses and the depleted fraction of the TiO_2 film can be observed in Fig. 4. In the case of the highest efficiency, the total depletion width (W_t) is the maximum and equals 395 nm; moreover, half of the TiO_2 film is depleted (depleted fraction is equal to 0.49), suggesting that the depletion region indeed assists in the charge separation and suppresses the back reaction, and consequently contributes to the increase in the power conversion efficiency of the cells. For the low efficiencies, the W_t is the lowest, and the depleted fraction of TiO_2 is around 0.1, which means that only 10% of the total TiO_2 thickness is depleted. Furthermore, there is good agreement between the open circuit voltage and the built-in potential observed from the Mott Schottky plot. In conclusion there is a very good agreement between the depletion region width and the PCE observed.

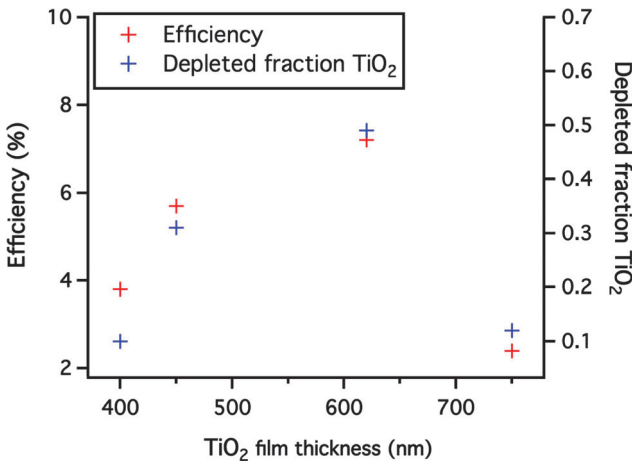

Fig. 4 Efficiency and depleted fraction of TiO_2 as a function of the TiO_2 film thickness.

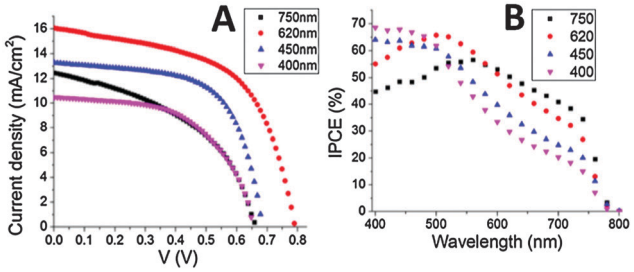

Fig. 5 (A) *JV* curves of the different TiO_2 film thickness for the hole conductor free perovskite solar cells and their (B) IPCE spectra.

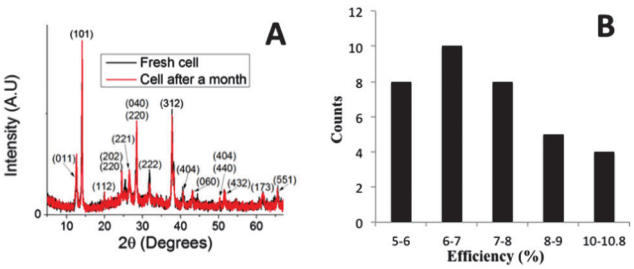

Fig. 6 (A) XRD diffraction of the fresh cell and the same cell after a month. About two third of the peaks belong to the orthorhombic structure of the $CH_3NH_3PbI_3$ perovskite, while one third belongs to the tetragonal structure of the $CH_3NH_3PbI_3$ perovskite. (B) Histogram of the $CH_3NH_3PbI_3$–TiO_2 heterojunction solar cells efficiency. The average efficiency is 7.7%, with more than 11% of the cells showing efficiencies above 10%.

The *JV* curves and the incident photon to current efficiency (IPCE) of the hole conductor free perovskite solar cells using various TiO_2 film thicknesses are presented in Fig. 5A and B.

Fig. 6A presents XRD diffraction of a fresh cell and the same cell (which stayed in the dark) after a month; the peaks in the figure are indexed according to ref. 25, while two third of the peaks belong to the orthorhombic structure of the $CH_3NH_3PbI_3$ perovskite, and one third belongs to the tetragonal structure of the $CH_3NH_3PbI_3$ perovskite. Moreover the peaks are matched completely between the two measurements, suggesting that there is no change in the crystallographic structure of the perovskite over time, which indicates the high stability of these hole conductor free perovskite solar cells. Fig. 6B shows the reproducibility of the $CH_3NH_3PbI_3$–TiO_2 heterojunction solar cells made using the optimum conditions describe above (TiO_2 thickness, wait time, blocking layer conditions). More than 45% of the cells show efficiencies above 8%, while more than 11% show efficiencies above 10%. The average power conversion efficiency is 7.7%.

Using the optimum conditions discussed in this paper, our best cell achieved a PCE of 10.85% with a V_{oc} of 0.84 V, a FF of 68% and a J_{sc} of 19 mA cm^{-2}. Its current density–voltage curve is presented in Fig. 7A. The corresponding IPCE spectra are shown in Fig. 7B, it reaches its maximum of 88% at 400 nm–600 nm wavelengths and gradually drops at longer wavelength

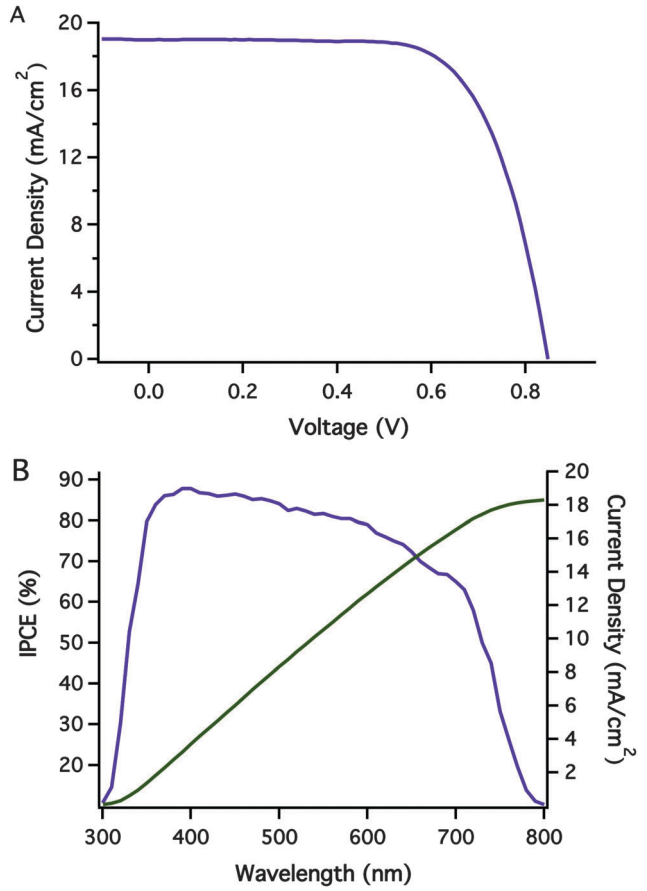

Fig. 7 (A) Current density–voltage curve of the champion hole conductor free $CH_3NH_3PbI_3$–TiO_2 heterojunction solar cell; (B) the corresponding IPCE spectrum and its integrated current density.

corresponding to its absorption spectrum. Without a hole conductor the charge carriers at the gold back contact aren't extracted efficiently, which influences the carrier collection at a longer wavelength (explains the decrease in the IPCE spectra from 600 nm wavelength). The integration of the IPCE spectra gives a current density of 18.3 mA cm^{-2} as shown in Fig. 7B, there is good agreement with the current density measured using the solar simulator. To the best of our knowledge, this is the highest efficiency reported for $CH_3NH_3PbI_3$ perovskite based solar cells without a hole transport material.

Conclusions

This work describes an in-depth study of the parameters influencing the PV performance of hole conductor free lead halide iodide solar cells. A two-step deposition technique of the perovskite was used, which assisted in achieving higher efficiencies. We have found a correlation between the depletion region width at the TiO_2–$CH_3NH_3PbI_3$ junction and the efficiency observed. The highest efficiency was achieved when half of the TiO_2 film was depleted. It was observed from the XRD analysis that the crystallographic structure does not change over time which supports the high stability of these cells. The best PCE achieved in this study was 10.85% which is, to date, the highest efficiency of these hole conductor free perovskite solar cells.

Experimental

Method and device fabrication

CH_3NH_3I was synthesized as described earlier[5] by reacting 30 mL of methylamine (40% in methanol, TCI) and 32.3 mL of hydroiodic acid (57 wt% in water, Aldrich) in a 250 mL round bottom flask at 0 °C for 2 h with stirring. The precipitate was recovered by putting the solution on a rotavap and carefully removing the solvents at 50 °C. The yellowish raw product of methylammonium iodide (CH_3NH_3I) was washed with ethanol by stirring the mixture for 30 min. Then the mixture was filtered and washed with diethylether. The washing step was repeated three times. After filtration, the solid was collected and dried at 60 °C in a vacuum oven for 24 h.

Device fabrication

The substrate of the device was a SnO_2:F(FTO) conducting glass (15 Ω cm^{-1}, Pilkington). A blocking layer was deposited on the FTO glass using a solution of titanium diisopropoxidebis(acetylacetonate)(TiDIP, 75% in isopropanol, Aldrich) in ethanol. Various volumetric ratios (0.05%, 0.10%, 0.15%, 0.20%) of the TiDIP solution were spin coated and then annealed at 450 °C for 35 min. Various dilutions of titania paste (20 nm, dyesol) were prepared by diluting the titania paste with ethanol at different weight ratios. The TiO_2 solution was spin coated and annealed at 500 °C for 30 min subsequent to $TiCl_4$ treatment for 30 min at 70 °C and annealing at 500 °C for 30 min.

The synthesis of $CH_3NH_3PbI_3$ on the TiO_2 surface was carried out by a two-step deposition technique as described previously[18] but with several modifications. At the beginning, PbI_2 was dropped onto the TiO_2 film and spin coated after various wait time periods (1 min, 1.5 min, 3 min, or 5 min) followed by annealing at 70 °C for 30 min. In the second step, the cell was dipped into 10 mg ml^{-1} of CH_3NH_3I solution at 70 °C for 20 s, and then annealed at 70 °C for another 30 min. During the dip and the annealing, $CH_3NH_3PbI_3$ was formed, indicated by the dark brown color of the electrode. Finally, the back contact was deposited by evaporating 50 nm of gold under a pressure of 5×10^{-6} Torr. The active area was 0.09 cm^2.

Profiler. The thickness measurements of the TiO_2 films were performed using a Veeco Dektak 150 profiler.

Extra high resolution scanning electron microscopy (XHR-SEM). Magellan XHR SEM was performed using a FEI (Field Emission Instruments), The Netherlands. The measurement conditions were 5 kV at a magnification of 100 000.

X-ray diffraction. X-ray powder diffraction measurements were performed in grazing incidence X-ray diffraction (GIXRD) mode on the D8 Advance diffractometer (Bruker AXS, Karlsruhe, Germany) with a goniometer radius of 217.5 mm, a secondary graphite monochromator, 2° Soller slits and a 0.2 mm receiving slit. XRD patterns within the range 5° to 60° 2θ were recorded at room temperature using CuKα radiation ($l\frac{1}{4}$ 1.5418 Å) with the

following measurement conditions: a tube voltage of 40 kV, a tube current of 40 mA, step-scan mode with a step size of 0.02° 2θ and a counting time of 1–3 s per step. The value of the grazing incidence angle was 2.5°.

Photovoltaic characterization. Photovoltaic measurements were made on a New Port system, composed of the Oriel *I–V* test station using an Oriel Sol3A simulator. The solar simulator is class AAA for spectral performance, uniformity of irradiance, and temporal stability. The solar simulator is equipped with a 450 W xenon lamp. The output power is adjusted to match AM1.5 global sunlight (100 mW cm^{-2}). The spectral match classifications are IEC60904-9 2007, JIC C 8912, and ASTM E927-05. *I–V* curves were obtained by applying an external bias to the cell and measuring the generated photocurrent using a Keithley model 2400 digital source meter. The voltage step and delay time of photocurrent were 10 mV and 40 ms, respectively. Oriel IQE-200 was used to determine the monochromatic incident photon-to-electric current conversion efficiency. Under full computer control, light from a 150 W xenon arc lamp was focused through a monochromator in the 300–1800 nm wavelength range onto the photovoltaic cell under investigation. The monochromator was incremented through the visible spectrum to generate the IPCE (λ) as defined by IPCE (λ) = 12 400 ($J_{sc}/\lambda\varphi$), where λ is the wavelength, J_{sc} is the short-circuit photocurrent density (mA cm^{-2}), and φ is the incident radiative flux (mW cm^{-2}). Photovoltaic performance was measured by using a metal mask with an aperture area of 0.09 cm^2.

Capacitance voltage measurements. The measurements were performed using a Metrohm Autolab system, equipped with a PGTSTAT302N potentiostat instrument. The frequency was 1 kHz at bias potentials between 0 and 0.9 V.

Acknowledgements

We would like to thank the Israel Alternative Energy Foundation (I-SAEF) that financed this research. We would like to thank Dr Vladimir Uvarov and Ms Evgenia Blayvas from the Harvey M. Krueger Center for Nanoscience and Nanotechnology at the Hebrew University for the XRD and the HR-SEM measurements, respectively.

References

1 A. Kojima, M. Ikegami, K. Teshima and T. Miyasaka, Highly Luminescent Lead Bromide Perovskite Nanoparticles Synthesized with Porous Alumina Media, *Chem. Lett.*, 2012, **41**, 397.

2 C. R. Kagan, D. B. Mitzi and C. D. Dimitrakopoulos, Organic-Inorganic Hybrid Materials as Semiconducting Channels in Thin-Film Field-Effect Transistors, *Science*, 1999, **286**, 945.

3 D. B. Mitzi, C. A. Feild, Z. Schlesinger and R. B. Laibowitz, Transport Optical and Magnetic properties of the conducting Halide Perovskite $CH_3NH_3SnI_3$, *J. Solid State Chem.*, 1995, **114**, 159.

4 A. Kojima, K. Teshima, Y. Shirai and T. Miyasaka, Organometal Halide Perovskites as Visible-Light Sensitizers for Photovoltaic Cells, *J. Am. Chem. Soc.*, 2009, **131**, 6050–6051.

5 J.-H. Im, J. Chung, S.-J. Kim and N.-G. Park, Synthesis, structure, and photovoltaic property of a nanocrystalline 2H perovskite-type novel sensitizer $(CH_3CH_2NH_3)PbI_3$, *Nanoscale Res. Lett.*, 2012, **7**, 353.

6 J.-H. Im, C.-R. Lee, J.-W. Lee, S. g-W. Park and N.-G. Park, 6.5% efficient perovskite quantum-dot-sensitized solar cell, *Nanoscale*, 2011, **3**, 4088.

7 H.-S. Kim, C.-R. Lee, J.-H. Im, K.-B. Lee, T. Moehl, A. Marchioro, S.-J. Moon, R. Humphry-Baker, J.-H. Yum, J. E. Moser, M. Grätzel and N.-G. Park, Lead Iodide Perovskite Sensitized All-Solid-State Submicron Thin Film Mesoscopic Solar Cell with Efficiency Exceeding 9%, *Nat. Sci. Rep.*, 2012, **2**, 591.

8 I. Chung, B. Lee, J. He, R. P. H. Chang and M. G. Kanatzidis, All-solid-state dye-sensitized solar cells with high efficiency, *Nature*, 2012, **485**, 486–489.

9 M. Lee, M. J. Teuscher, T. Miyasaka, T. N. Murakami and H. J. Snaith, Efficient Hybrid Solar Cells Based on Meso-Superstructured Organometal Halide Perovskites, *Science*, 2012, **338**, 643–644.

10 J. M. Ball, M. M. Lee, A. Hey and H. J. Snaith, Low-temperature processed meso-superstructured to thin-film perovskite solar cells, *Energy Environ. Sci.*, 2013, **6**(6), 1739–1743.

11 J. H. Heo, S. H. Im, J. H. Noh, T. N. Mandal, C.-S. Lim, J. A. Chang, Y. H. Lee, H.-j. Kim, A. Sarkar, M. K. Nazeeruddin, M. Grätzel and S. I. Seok, Efficient inorganic–organic hybrid heterojunction solar cells containing perovskite compound and polymeric hole conductors, *Nat. Photonics*, 2013, **7**, 486–491.

12 B. Cai, Y. Xing, Z. Yang, W.-H. Zhang and J. Qiu, High performance hybrid solar cells sensitized by organolead halide perovskites, *Energy Environ. Sci.*, 2013, **6**, 1480.

13 E. Edri, S. Kirmayer, D. Cahen and G. Hodes, High Open-Circuit Voltage Solar Cells Based on Organic–Inorganic Lead Bromide Perovskite, *J. Phys. Chem. Lett.*, 2013, **4**(6), 897–902.

14 H.-S. Kim, I. Mora-Sero, V. Gonzalez-Pedro, F. Fabregat-Santiago, E. J. Juarez-Perez, N.-G. Park and J. Bisquert, Mechanism of carrier accumulation in perovskite thin-absorber solar cells, *Nat. Commun.*, 2013, DOI: 10.1038/ncomms3242.

15 E. Mosconi, A. Amat, Md. K. Nazeeruddin, M. Grätzel and F. De Angelis, First-Principles Modeling of Mixed Halide Organometal Perovskites for Photovoltaic Applications, *J. Phys. Chem. C*, 2013, **117**, 13902–13913.

16 S. D. Stranks, G. E. Eperon, G. Grancini, C. Menelaou, M. J. P. Alcocer, T. Leijtens, L. M. Herz, A. Petrozza and H. J. Snaith, Electron-Hole Diffusion Lengths Exceeding 1 Micrometer in an Organometal Trihalide Perovskite Absorber, *Science*, 2013, **342**, 341.

17 G. Xing, N. Mathews, S. Sun, S. S. Lim, Y. M. Lam, M. Grätzel, S. Mhaisalkar and T. C. Sum, Long-Range

Balanced Electron- and Hole-Transport Lengths in Organic-Inorganic $CH_3NH_3PbI_3$, *Science*, 2013, **342**, 344.

18 J. Burschka, N. Pellet, S.-J. Moon, R. Humphry-Baker, P. Gao, Md. K. Nazeeruddin and M. Grätzel, Sequential deposition as a route to high-performance perovskite-sensitized solar cells, *Nature*, 2013, **499**, 316.

19 M. Liu, M. B. Johnston and H. J. Snaith, Efficient planar heterojunction perovskite solar cells by vapour deposition, *Nature*, 2013, **501**, 395–398.

20 L. Etgar, P. Gao, Z. Xue, Q. Peng, A. K. Chandiran, B. Liu, Md. K. Nazeeruddin and M. Grätzel, Mesoscopic $CH_3NH_3PbI_3$/TiO_2 Heterojunction Solar Cells, *J. Am. Chem. Soc.*, 2012, **134**, 17396–17399.

21 W. A. Laben and L. Etgar, Depleted hole conductor-free lead halide iodide heterojunction solar cell, *Energy Environ. Sci.*, 2013, **6**, 3249–3253.

22 J. Shi, J. Dong, S. Lv, Y. Xu, L. Zhu, J. Xiao, X. Xu, H. Wu, D. Li, Y. Luo and Q. Meng, *Appl. Phys. Lett.*, 2014, **104**, 063901.

23 W. Schottky, Vereinfachte und Erweiterte Theorie der Randschicht-Gleichrichter, *Z. Phys.*, 1942, **118**, 539–592.

24 J. P. Clifford, K. W. Johnston, L. Levina and E. H. Sargent, Schottky barriers to colloidal quantum dot films, *Appl. Phys. Lett.*, 2007, **91**, 253117.

25 A. Poglitsch and D. Weber, Dynamic disorder in methylammoniumtrihalogenoplumbates(II) observed by millimeter-wave spectroscopy, *J. Chem. Phys.*, 1987, **87**(11), 6373–6378.

26 T. Baikie, Y. Fang, J. M. Kadro, M. Schreyer, F. Wei, S. G. Mhaisalkar, M. Graetzel and T. J. White, Synthesis and crystal chemistry of the hybrid perovskite $(CH_3NH_3)PbI_3$ for solid-state sensitised solar cell applications, *J. Mater. Chem. A*, 2013, **1**, 5628–5641.

27 J. M. Luther, M. Law, M. C. Beard, Q. Song, M. O. Reese, R. J. Ellingson and A. J. Nozik, Schottky Solar Cells Based on Colloidal Nanocrystal Films, *Nano Lett.*, 2008, **8**(10), 3488–3492.

28 B. O'Regan, J. Moser, M. Anderson and M. Graetzel, Vectorial electron injection into transparent semiconductor membranes and electric field effects on the dynamics of light-induced charge separation, *J. Phys. Chem.*, 1990, **94**, 8720–8726.

29 S. Nakade, Y. Saito, W. Kubo, T. Kanzaki, T. Kitamura, Y. Wada and S. Yanagida, Enhancement of electron transport in nano-porous TiO_2 electrodes by dye adsorption, *Electrochem. Commun.*, 2003, **5**, 804–808.

30 A. Zaban, A. Meier and B. A. Gregg, Electric Potential Distribution and Short-Range Screening in Nanoporous TiO_2 Electrodes, *J. Phys. Chem. B*, 1997, **101**, 7985–7990.